RSC Advances

ROYAL SOCIETY OF CHEMISTRY

www.rsc.org/advances

Conversion of broadband UV-visible light to near infrared emission by $Ca_{14}Zn_6Al_{10}O_{35}$: Mn^{4+}, Nd^{3+}/Yb^{3+}

Xuejun Gao,[†] Wenbin Xia,[†] Tiejin Chen,[†] Xiaoliang Yang,[†] Xiangliang Jin[†] and Siguo Xiao[*†]

[†]School of Physics and Optoelectronics, Xiangtan University, Hunan 411105, China

ABSTRACT: Efficient $Ca_{14}Zn_6Al_{10}O_{35}$: Mn^{4+}, Nd^{3+}/Yb^{3+} spectral conversion materials have been prepared by a sol-gel method. The $Ca_{14}Zn_6Al_{10}O_{35}$: Mn^{4+}, Nd^{3+}/Yb^{3+} materials can efficiently shift the short-wavelength sunlight in 250-550 nm spectral regions into near infrared emission which matches the higher sensitivity region of Si-based solar cell. The maximal energy transfer efficiency is 76.0% and 80.4% in Mn^{4+}, Nd^{3+} and Mn^{4+}, Yb^{3+} co-doped sample when excited at 460 nm, respectively. A dipole-dipole interaction is responsible for the energy transfer sensitization processes from Mn^{4+} to Nd^{3+}/Yb^{3+} ion, which has been confirmed by Dexter's theory and Yokota-Tanimoto model.

1. INTRODUCTION

Solar energy is free, clean and abundant in the world and thus is regarded as an ideal replaceable energy for mankind in the future. The capacity of photovoltaic device to transform sunlight directly into electricity promises a prime technology for solar energy utilization. Currently, the photovoltaic solar cell market is predominated by single-junction crystalline and polycrystalline Si solar cell with a conversion efficiency of about 15%.[1, 2] Nevertheless, the theoretical maximum conversion efficiency of Si-based solar cell is higher than 30%.[3, 4] In principle, photons with energy higher than the bandgap of photovoltaic devices are absorbed, but the Si-based solar cell works most efficiently under irradiation of the light in the vicinity of 1000 nm.

To enhance the efficiency of Si-based solar cell, down-shifting is a promising technique by which short-wavelength sunlight can be converted to light in near-infrared (NIR) region where the photovoltaic solar cell is more sensitive. Lanthanide ions were usually used to obtain NIR light by down shifting because of their rich energy-level structure permitting abundant NIR emission. Among the lanthanide ions, Nd^{3+} and Yb^{3+} are particularly noteworthy because their NIR emissions take place at around 900(1060) nm and 980 nm, respectively, which are just above the band edge of Si semiconductor where the solar cell exhibits excellent spectral response. However, the Nd^{3+} and Yb^{3+} ions exhibit weak and narrow absorption due to their parity-forbidden 4f-4f transitions, and as a result, only a small part of ultraviolet and visible sunlight can be converted into NIR emission. In order to realize broadband spectral conversion,

the f-d transition lanthanide ions (e.g., Ce^{3+}, Eu^{2+}, Yb^{2+}),[5, 6] transition metal ions (e.g., Cr^{3+}, Mn^{2+})[7-9] and semiconductor quantum dots (e.g., CdSe)[10-12] have been widely attempted as sensitizers in Nd^{3+}/Yb^{3+} doped materials. Nevertheless, enhancing the sensitized Nd^{3+}/Yb^{3+} NIR emission with excitation at UV-visible light is still a difficult problem to be solved.

In recent years, tetravalence manganese ion (Mn^{4+}) doped luminescent materials have been investigated and attracted much attention.[13-22] Mn^{4+} ions enter into the octahedral sites as substitutes and exhibit deep red luminescence.[18, 19, 23] More importantly, the Mn^{4+}-O^{2-} charge transfer transition and $^4A_2 \rightarrow {}^4T_1$, $^4A_2 \rightarrow {}^4T_2$ spin-allowed d-d transitions of Mn^{4+} exhibit a strong and continuous UV and visible absorption, which indicates the possible application for broadband light conversion. Among these phosphors, the Mn^{4+} doped $Ca_{14}Zn_6Al_{10}O_{35}$ material is especially attractive because of its high luminescence quantum efficiency, good thermal and chemical stability, and ease of preparation.[13, 22] Furthermore, the Ca^{2+} sites can be replaced by Nd^{3+}/Yb^{3+} ions because of their similar ion radius. This implies that efficient energy transfer from Mn^{4+} to Nd^{3+}/Yb^{3+} can possibly take place in the $Ca_{14}Zn_6Al_{10}O_{35}$ matrix. Hence the Mn^{4+}, Nd^{3+}/Yb^{3+} co-doped $Ca_{14}Zn_6Al_{10}O_{35}$ materials promise to be broadband spectral converters to obtain efficient NIR emission (around 1000 nm).

In this paper, two spectral conversion materials, i.e., $Ca_{14}Zn_6Al_{10}O_{35}$: Mn^{4+}, Nd^{3+} and $Ca_{14}Zn_6Al_{10}O_{35}$: Mn^{4+}, Yb^{3+} have been prepared. The luminescence properties and energy transfer mechanism between Mn^{4+} and Nd^{3+}/Yb^{3+} ions were investigated in detail.

2. EXPERIMENTAL

2.1. Materials synthesis

The spectral conversion materials were prepared through a sol-gel procedure. $Al(NO_3)_3(H_2O)_9$ (99.9%), $Nd(NO_3)_3(H_2O)_6$ (99.9%), $Yb(NO_3)_3(H_2O)_6$ (99.9%), $Mn(NO_3)_2(H_2O)_4$ (99.9%), $Ca(NO_3)_2(H_2O)_4$ (99.9%), $Zn(NO_3)_2(H_2O)_6$ (99.9%), $C_6H_8O_7$ (99.9%) were used as raw materials. Firstly, the reagents were dissolved in distilled water with the stoichiometric ratio of $Ca_{14-x/y}Zn_6Al_{10-z}O_{35}$: Mn_z, Nd_x/Yb_y (x = 0.00, 0.05, 0.10, 0.15, 0.20, 0.225, 0.25, 0.275, 0.30, 0.40; y = 0.0, 0.2, 0.4, 0.6, 0.7, 0.8, 0.9, 1.0, 1.2; z = 0.0, 0.2, 0.4, 0.5, 0.55, 0.6, 0.65, 0.7, 0.8, 1.0) and subsequently mixed by stirring. Then the $C_6H_8O_7$ aqueous solutions were dripped into the nitrate solutions with the cation-ligand ratio cation : $C_6H_8O_7$ = 1 : 1.5 accompanied by constant stirring. After standing for 12 h, the solutions were dried at 100 °C for 24 hours to obtain precursors. Then the precursors were carried out to remove the organic matter by heating the temperature to 600 °C for 2 h and then cooled to room temperature. After grinding, the powders were heated to 1000 °C with a ramp rate of 5 °C/min under air condition and calcined at that temperature for 2 h to obtain the final products.

2.2. Characterization

The crystalline phases of the samples were analyzed by X-ray diffraction (XRD) on a Bruker D8 advanced equipment, using Cu tube with Cu/K (k = 0.1541 nm) radiation. X-ray photoelectron spectroscopy (XPS) was measured on a K-Alpha 1063 (Thermo Fisher Scientific) with a focused monochromatic Al Ka X-ray beam (12 kV, 6 mA, 5×10^{-9} torr). The

photoexcitation spectra (PLE) and visible-near-infrared photoluminescence (PL) spectra were measured by a monochromator (Zolix Instrument, Omni-λ320i) coupled with photomultiplier (PMTH-S1-CR131) and near infrared sensitive detector (DInGaAs 2600-TE), in which a monochromator (Zolix Instrument Omni-λ320) coupled with a 150 W xenon lamp was used to provide the monochromatic exciting light. The luminescence decay curves were analyzed by a PTI QM 40 spectrofluorometer, using a pulse xenon lamp as the excitation source. The diffuse refection spectra of the samples were measured by a Varian Cary 100 UV-Vis Spectrofluorometer with a DRA-CA-30I Diffuse Reflectance Accessory. The morphology of the prepared samples was characterized by a JSM-6610 scanning electron microscope (SEM).

3. RESULTS AND DISCUSSION

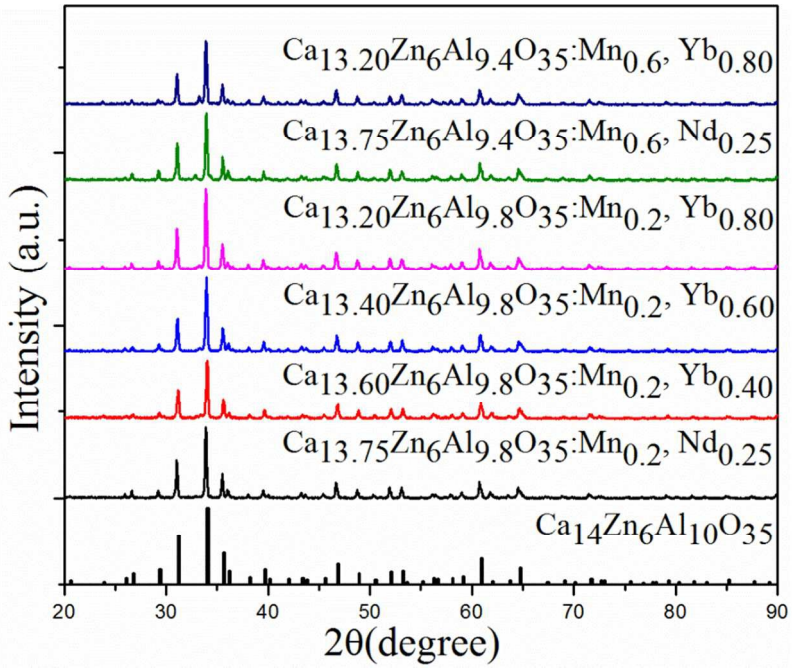

Figure 1. Power X-ray diffraction patterns of $Ca_{14-x/y}Zn_6Al_{10-z}O_{35}$: Mn_z, Nd_x/Yb_y (x = 0.25, y =

0.4, 0.6, 0.8, z = 0.2, 0.6).

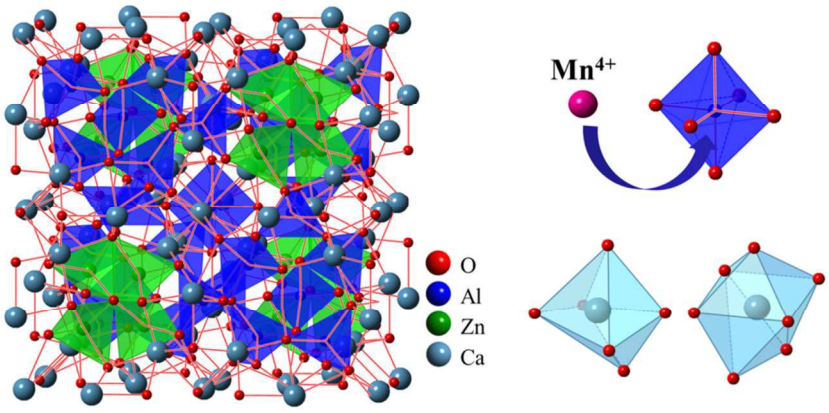

Figure 2. Schematic of the $Ca_{14}Zn_6Al_{10}O_{35}$ crystal structure.

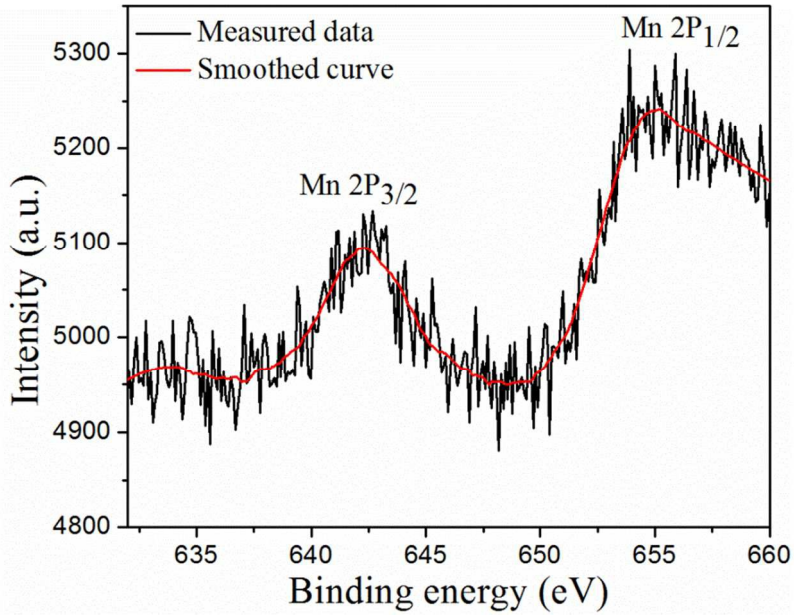

Figure 3. Mn 2p XPS spectrum of $Ca_{14}Zn_6Al_{9.4}O_{35}$: $Mn_{0.6}$ sample.

Figure 1 shows the X-ray diffraction (XRD) patterns of $Ca_{14-x/y}Zn_6Al_{10-z}O_{35}$: Mn_z, Nd_x/Yb_y (x = 0.25, y = 0.4, 0.6, 0.8, z = 0.2, 0.6). The diffraction peaks of the samples can be identified by comparison with the standard XRD data of $Ca_{14}Zn_6Al_{10}O_{35}$ (JCPDS 50-0426). $Ca_{14}Zn_6Al_{10}O_{35}$ has a cubic structure with space group F23. In $Ca_{14}Zn_6Al_{10}O_{35}$ crystal structure,

four of the five independent positions occupied by Zn and Al are in the tetrahedral coordination，with the average Zn-O distances of 1.951 Å and average Al-O distances of 1.719, 1.794 and 1.891 Å, respectively. The fifth independent position is in the octahedral coordination with the Al-O distance of 1.936 Å. In addition, Ca^{2+} has three different coordination environments. Two of them are in octahedral with the average Ca-O distances of 2.336 and 2.346 Å, and the third independent Ca^{2+} is in a seven-coordinated polyhedron with an average Ca-O distance being equal to 2.498 Å.[24] The schematic of $Ca_{14}Zn_6Al_{10}O_{35}$ crystal structure is shown in Figure 2. Figure 3 shows the Mn XPS core level spectrum for $Ca_{14}Zn_6Al_{9.4}O_{35}$: $Mn_{0.6}$. The smoothed XPS spectrum shows the peak of Mn $2p_{3/2}$ with a binding energy at 642.3 eV (see Figure 3). It is known that the peaks of Mn^{2+} $2p_{3/2}$ (MnO), Mn^{3+} $2p_{3/2}$ (Mn_2O_3) and Mn^{4+} $2p_{3/2}$ (MnO_2) locate at 641.7, 641.8 and 642.4 eV, respectively.[25] Therefore, the Mn element predominantly behaves as the state of Mn^{4+} in the $Ca_{14}Zn_6Al_{10}O_{35}$ host. It is commonly accepted that Mn^{4+} ions are preferentially accommodated at the Al^{3+} sites in the lattice with an octahedral coordination.[13, 22] It can be seen that Ca^{2+} site is likely to be replaced by Nd^{3+}/Yb^{3+} ion without significant structural changes when a small amount of Nd^{3+}/Yb^{3+} are introduced, due to the similar ion radius between Ca^{2+} and Nd^{3+}/Yb^{3+} (Ca^{2+} : radius = 0.100 nm; Nd^{3+} : radius = 0.098 nm; Yb^{3+} : radius = 0.086 nm). Considering the different valences of Ca^{2+} and Nd^{3+}/Yb^{3+}, charge compensation is required. The commonly accepted view is that the formative Ca vacancies can compensate charge imbalance.[26-28] When Nd^{3+}/Yb^{3+} ions are co-doped into $Ca_{14}Zn_6Al_{10}O_{35}$ matrix, the Ca vacancies might form and they could keep the electroneutrality of the compound.

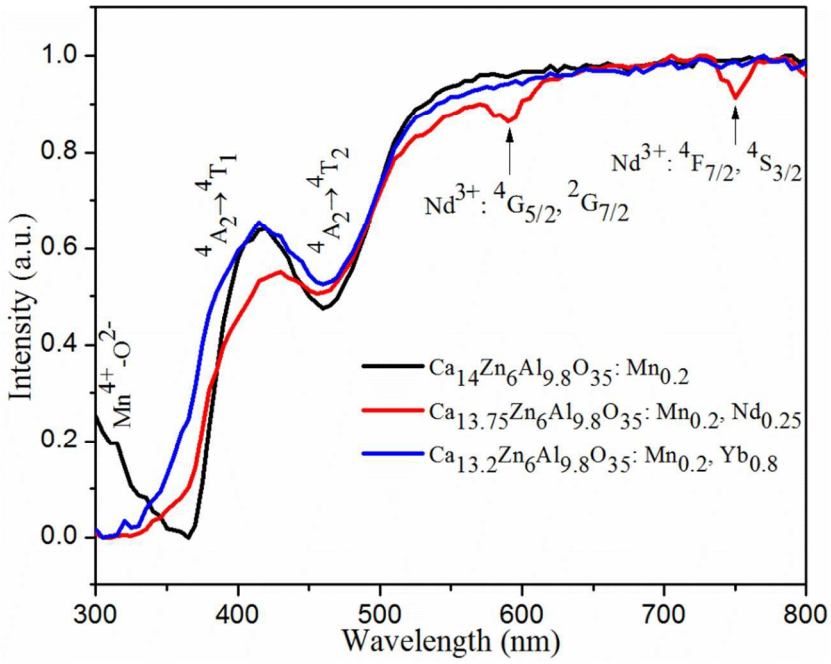

Figure 4. Normalized diffuse reflection spectra of $Ca_{14}Zn_6Al_{9.8}O_{35}$:$Mn_{0.2}$, $Ca_{13.75}Zn_6Al_{9.8}O_{35}$:$Mn_{0.2}$, $Nd_{0.25}$ and $Ca_{13.2}Zn_6Al_{9.8}O_{35}$:$Mn_{0.2}$, $Yb_{0.8}$ samples.

The diffuse reflection spectra of $Ca_{14}Zn_6Al_{10}O_{35}$ doped with Mn^{4+}, Nd^{3+} and Yb^{3+} ions are shown in Figure 4. In the Mn^{4+} single-doped and Mn^{4+}, Nd^{3+}/Yb^{3+} co-doped samples, it can be seen two strong absorption peaks at 370 nm and 465 nm originating from the spin-allowed Mn^{4+}: $^4A_2 \rightarrow {}^4T_1$ and Mn^{4+}: $^4A_2 \rightarrow {}^4T_2$ transitions, which are similar to the experimental results reported previously[29]. The absorption band between 300 and 350 nm is due to the charge transfer transition of Mn^{4+}-O^{2-}. In addition, the weak and narrow absorption peaks of Nd^{3+} are also observed in $Ca_{14}Zn_6Al_{10}O_{35}$:Mn^{4+}, Nd^{3+}. The high absorption efficiency of the above mentioned samples in the wide UV-visible light region are beneficial to the realization of the short-wavelength light down-shifting.

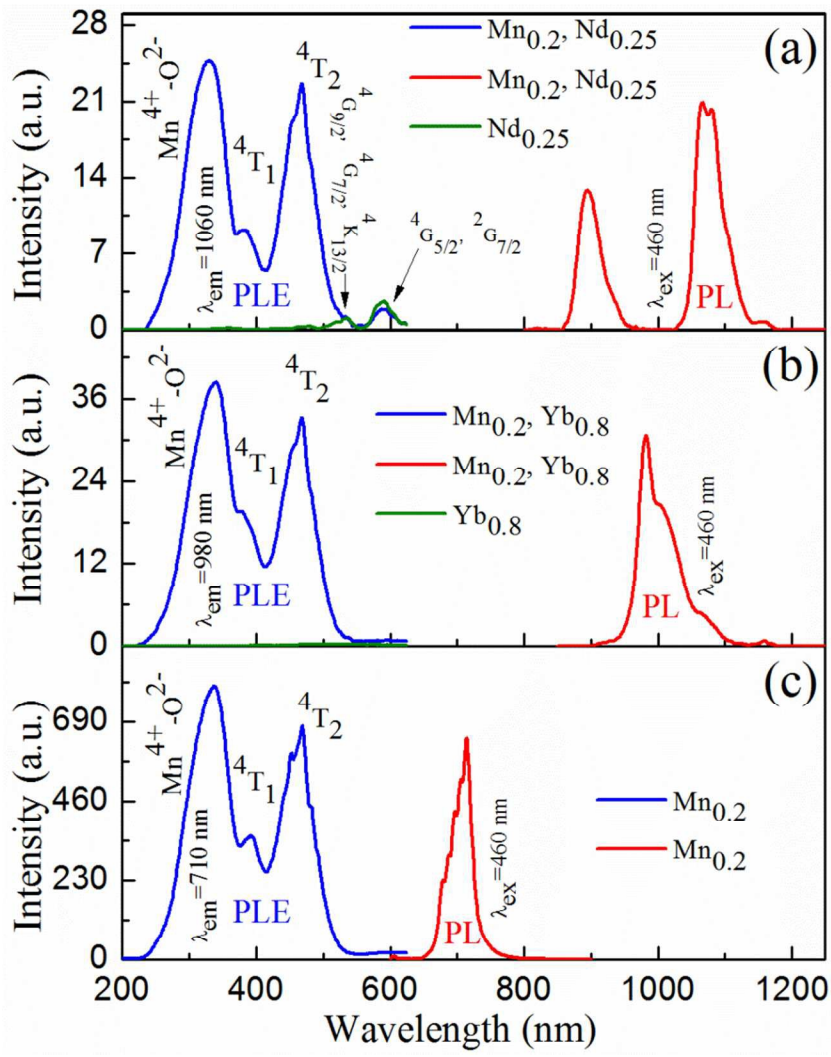

Figure 5. PLE spectra (left) and/or PL spectra (right) for the $Ca_{13.75}Zn_6Al_{9.8}O_{35}$: $Mn_{0.2}$, $Nd_{0.25}$ and $Ca_{13.75}Zn_6Al_{10}O_{35}$: $Nd_{0.25}$ samples (a), the $Ca_{13.2}Zn_6Al_{9.8}O_{35}$: $Mn_{0.2}$, $Yb_{0.8}$ and $Ca_{13.2}Zn_6Al_{10}O_{35}$: $Yb_{0.8}$ samples (b), and the $Ca_{14}Zn_6Al_{9.8}O_{35}$: $Mn_{0.2}$ samples (c).

Figure 5 presents the normalized PLE and/or PL spectra of Mn^{4+}, Nd^{3+}, Yb^{3+} single-doped, Mn^{4+}, Nd^{3+}/Yb^{3+} co-doped samples. Excitation into the absorption band at 460 nm gives an intense broad red emission around 710 nm originating from the $^2E \rightarrow {}^4A_2$ spin-forbidden transition of Mn^{4+} ions in Mn^{4+} single-doped sample. The excitation also gives luminescence

bands which are located at 900, 1060 nm in Mn^{4+}, Nd^{3+} co-doped and 980 nm in Mn^{4+}, Yb^{3+} co-doped samples, originating from Nd^{3+}: $^4F_{3/2}\rightarrow{}^4I_{9/2}$, Nd^{3+}: $^4F_{3/2}\rightarrow{}^4I_{11/2}$ and Yb^{3+}: $^2F_{5/2}\rightarrow{}^2F_{7/2}$ transitions, respectively. The PLE spectra monitored at 710 nm of Mn^{4+} single-doped sample shows three broad peaks around 320, 380 and 470 nm, which can be attributed to the charge transfer transition of Mn^{4+}-O^{2-} and spin-allowed transitions of Mn^{4+}: $^4A_2\rightarrow{}^4T_1$, Mn^{4+}: $^4A_2\rightarrow{}^4T_2$ corresponding well with the absorption spectrum. It is noteworthy that the PLE spectra shapes of the Mn^{4+}, Nd^{3+} co-doped sample monitored at 1060 nm and the Mn^{4+}, Yb^{3+} co-doped sample monitored at 980 nm are quite similar to the Mn^{4+} single-doped sample (see Figure 5(a)-5(c)). Only weak and discrete PLE peaks in visible region caused by the f-f transitions of Nd^{3+} appear in the Nd^{3+} single-doped sample and no PLE peak in visible region is observed in the Yb^{3+} single-doped sample (see Figure 5(a) and 5(b)). Obviously, the typical broad and intense excitation bands in the Mn^{4+}, Nd^{3+}/Yb^{3+} co-doped samples monitored at the NIR region also originate from the charge transfer transition of Mn^{4+}-O^{2-} and spin-allowed transitions of Mn^{4+}: $^4A_2\rightarrow{}^4T_1$, Mn^{4+}: $^4A_2\rightarrow{}^4T_2$. The characteristics of the above PLE spectra demonstrate that the NIR luminescence of Nd^{3+}/Yb^{3+} in Mn^{4+}, Nd^3/Yb^{3+} co-doped samples is generated by the energy transfer sensitization from Mn^{4+} to Nd^{3+}/Yb^{3+} ions.

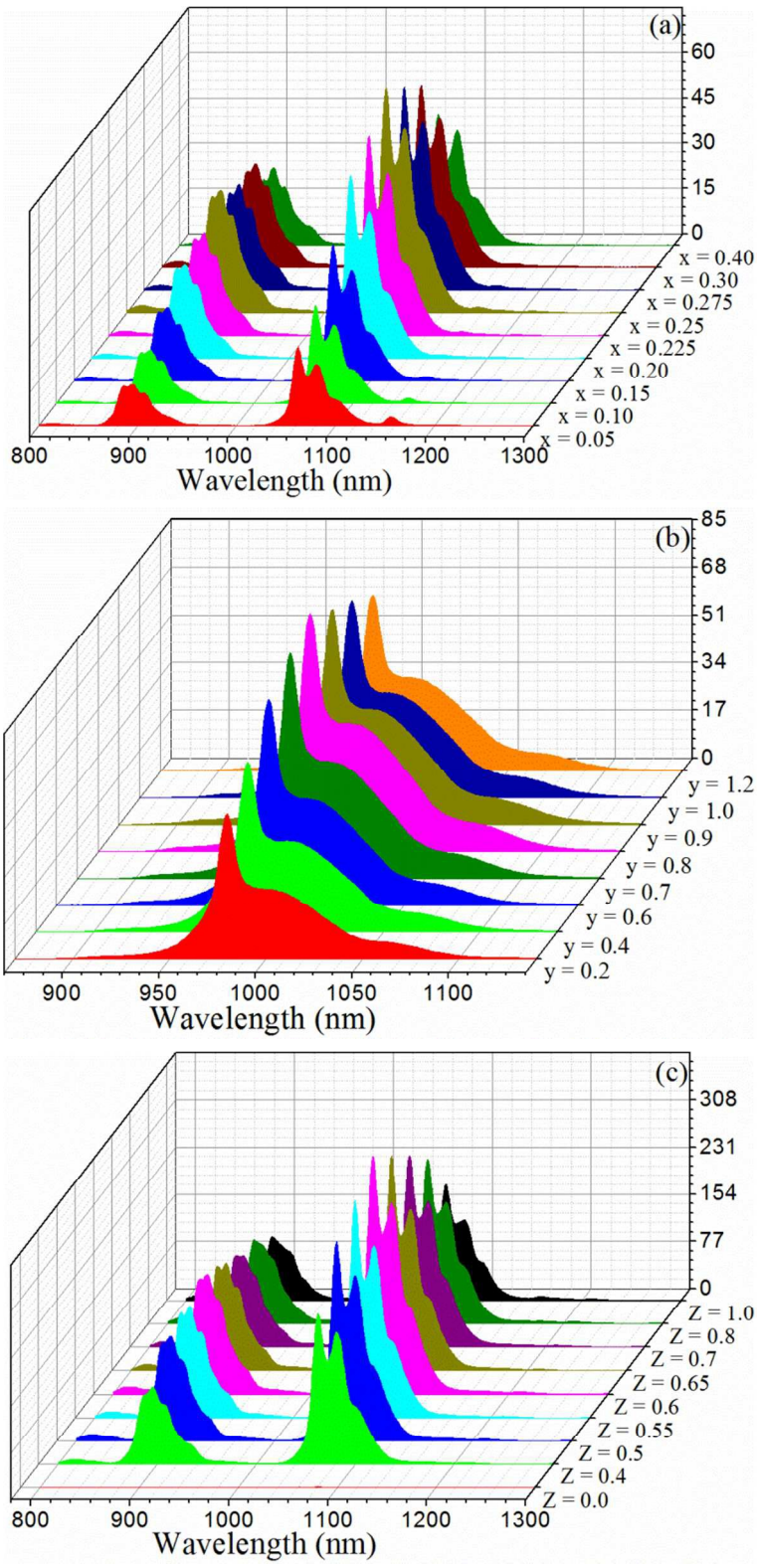

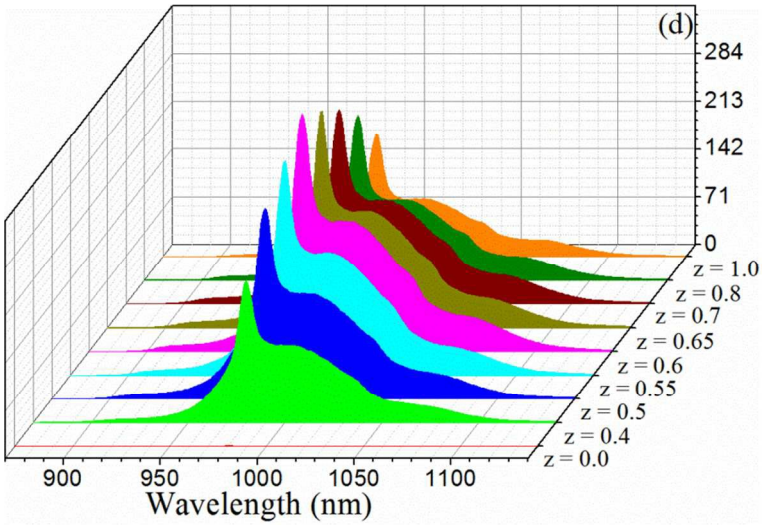

Figure 6. PL spectra of $Ca_{14-x}Zn_6Al_{9.8}O_{35}$: $Mn_{0.2}$, Nd_x (a), $Ca_{14-y}Zn_6Al_{9.8}O_{35}$: $Mn_{0.2}$, Yb_y (b), $Ca_{13.75}Zn_6Al_{10-z}O_{35}$: Mn_z, $Nd_{0.25}$ (c) and $Ca_{13.2}Zn_6Al_{10-z}O_{35}$: Mn_z, $Yb_{0.8}$ (d) excited at 460 nm.

In order to optimize the NIR emission performance, the PL for the $Ca_{14-x/y}Zn_6Al_{10-z}O_{35}$: Mn_z, Nd_x/Yb_y materials with different Mn^{4+} and Nd^{3+}/Yb^{3+} doping concentrations were systemically investigated under excitation at 460 nm. When the Mn^{4+} content is fixed (z = 0.2), it is found that the NIR PL intensity in both the Mn^{4+}, Nd^{3+} co-doped and Mn^{4+}, Yb^{3+} co-doped samples increases at first with the increase of the content of rare earth ions, reaching the maximum at x = 0.25 and y = 0.8, respectively, and then decreases gradually as the result of the concentration quenching, just as shown in Figure 6(a) and 6(b). When the Nd^{3+} and Yb^{3+} doping contents are fixed at x = 0.25 and y = 0.8, the NIR PL intensity of Nd^{3+} and Yb^{3+} can be further enhanced significantly by increasing the Mn^{4+} doping content (see Figure 6(c) and 6(d)), respectively. The NIR emission intensities of the Nd^{3+} and Yb^{3+} ions both reach their maximum at z = 0.6. Compared with the $Ca_{13.75}Zn_6Al_{10}O_{35}$: $Nd_{0.25}$ and $Ca_{13.2}Zn_6Al_{10}O_{35}$: $Yb_{0.8}$ samples, the NIR luminescence intensity is enhanced by 338 times at 1060 nm for $Ca_{13.75}Zn_6Al_{9.4}O_{35}$:$Mn_{0.6}$, $Nd_{0.25}$

and 306 times at 980 nm for $Ca_{13.2}Zn_6Al_{9.4}O_{35}:Mn_{0.6}$, $Yb_{0.8}$, respectively. The enhancement of the NIR emission induced by co-doped Mn^{4+} indicates the efficient energy transfer from Mn^{4+} to Nd^{3+}/Yb^{3+} ions.

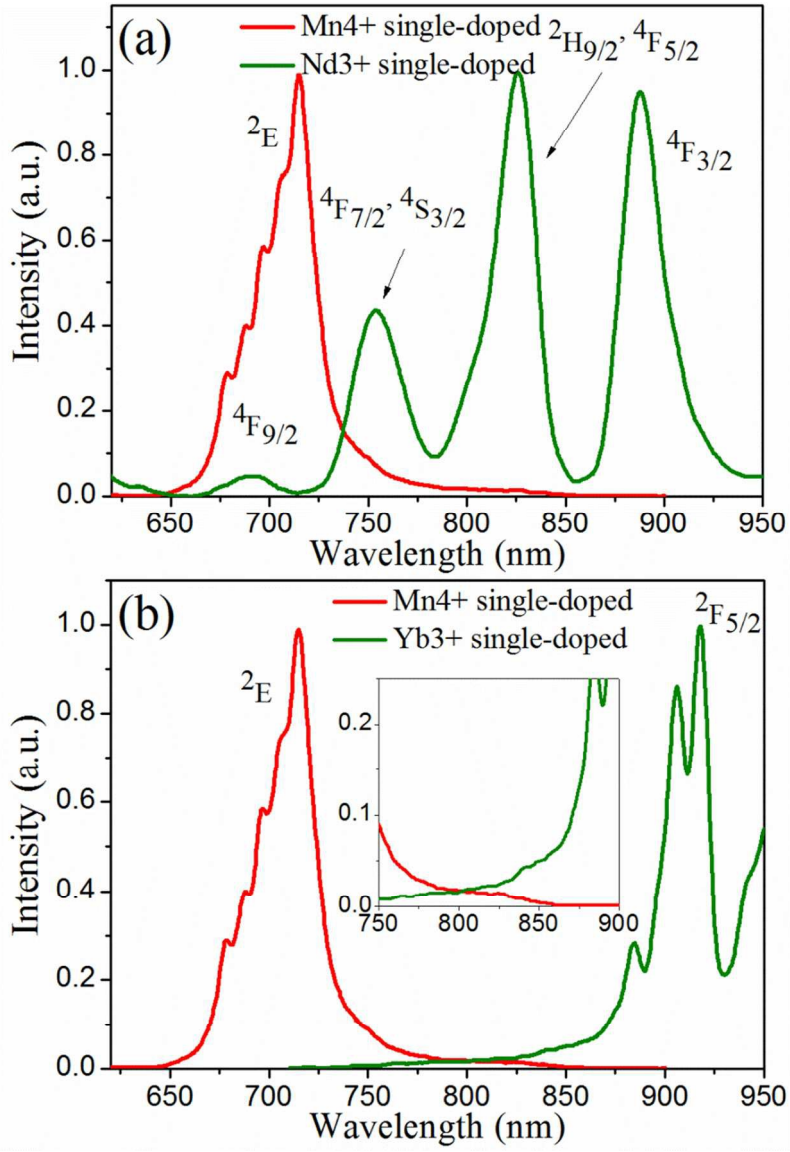

Figure 7. The overlapping between the emission spectra of Mn^{4+} and the excitation spectra of Nd^{3+} monitored at 1060 nm (a)/Yb^{3+} monitored at 980 nm (b).

The energy transfer efficiency depends on how well the acceptor energy levels match the frequencies of the donor emission. As we compare the emission spectra of Mn^{4+} single-doped

sample with the excitation spectra of Nd^{3+} single-doped sample, we can find a good spectral overlap between the Mn^{4+}: ^2E emission and the Nd^{3+}: $^4F_{9/2}$, $^4F_{7/2}$, $^4S_{3/2}$ excitation, as shown in Figure 7(a). Therefore, it enables the efficient sensitization NIR emission by nonradiative resonant energy transfer from Mn^{4+} to Nd^{3+} ions via the process Mn^{4+}: ^2E + Nd^{3+}: $^4I_{9/2}$→Mn^{4+}: $^4A_2$ + Nd^{3+}: $^4F_{9/2}$, $^4F_{7/2}$, $^4S_{3/2}$. From Figure 7(b), and we can see that there is relatively large energy gap between the Mn^{4+}: ^2E level and Yb^{3+}: $^2F_{5/2}$ level. It seems that efficient sensitization NIR emission by resonant energy transfer from Mn^{4+} to Yb^{3+} is unlikely. However, efficient energy transfer from Mn^{4+} to Yb^{3+} can still take place in the Mn^{4+}, Yb^{3+} co-doped samples. From the emission spectrum of Mn^{4+}: ^2E→$^4A_2$ shown in Figure 7(b), we can see that the emission sideband almost extends from the peak at 715 nm to 850 nm, which indicates the strong electron-phonon coupling in $Ca_{14}Zn_6Al_{10}O_{35}$. The strong electron-phonon coupling is beneficial to the phonon-assisted energy transfer.[30] Therefore the NIR luminescence of Yb^{3+} might be mainly generated by phonon-assisted energy transfer from Mn^{4+} to Yb^{3+}.

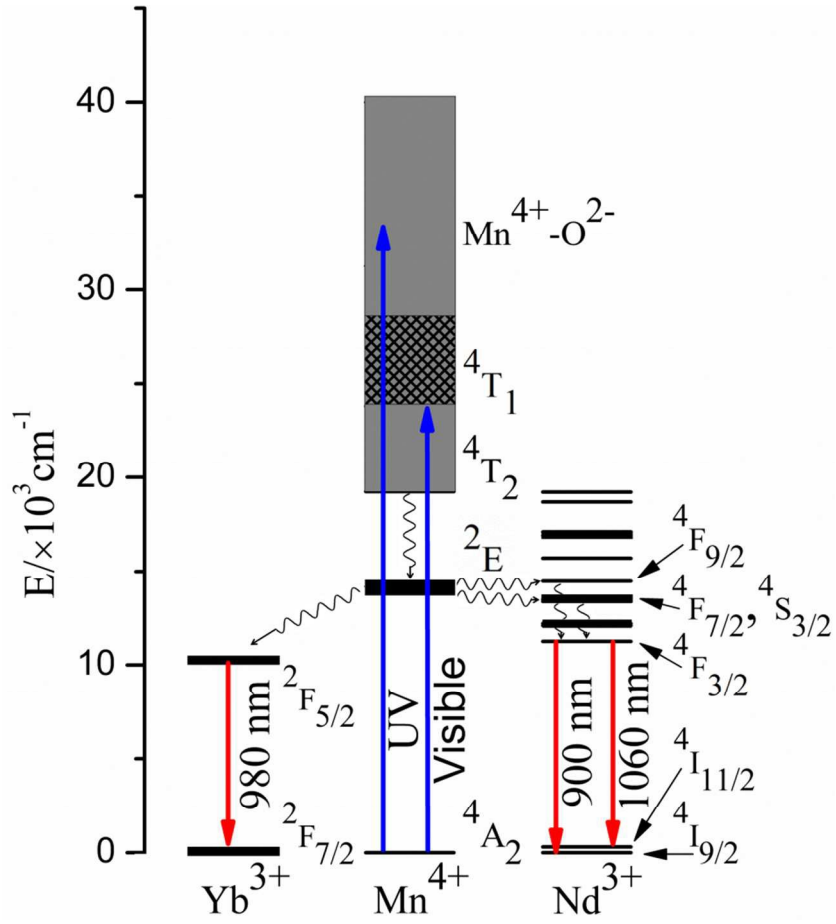

Figure 8. Energy-transfer and electron-transition scheme of Mn^{4+}, Nd^{3+}/Yb^{3+} in $Ca_{14}Zn_6Al_{10}O_{35}$.

The excitation/emission and energy transfer pathways for the Mn^{4+}, Nd^{3+}/Yb^{3+} ion couples in $Ca_{14}Zn_6Al_{10}O_{35}$ are illustrated in Figure 8. Firstly, the Mn^{4+} ions are excited into their charge-transfer or $^4T_1$, $^4T_2$ excited states by the irradiation. Then the excited Mn^{4+} ions rapidly relax to their metastable ^2E state, and the energy transfer takes place via Mn^{4+}: ^2E + Nd^{3+}: $^4I_{9/2} \rightarrow Mn^{4+}$: $^4A_2$ + Nd^{3+}: $^4F_{9/2}$, $^4F_{7/2}$, $^4S_{3/2}$ or Mn^{4+}: ^2E + Yb^{3+}: $^2F_{7/2} \rightarrow Mn^{4+}$: $^4A_2$ + Yb^{3+}: $^2F_{5/2}$. The following nonradiative relaxation among the intra-4f shell energy levels performs the population of Nd^{3+}: $^4F_{3/2}$ and Yb^{3+}: $^2F_{5/2}$ levels, resulting in the 900, 1060 and 980 nm emissions, respectively.

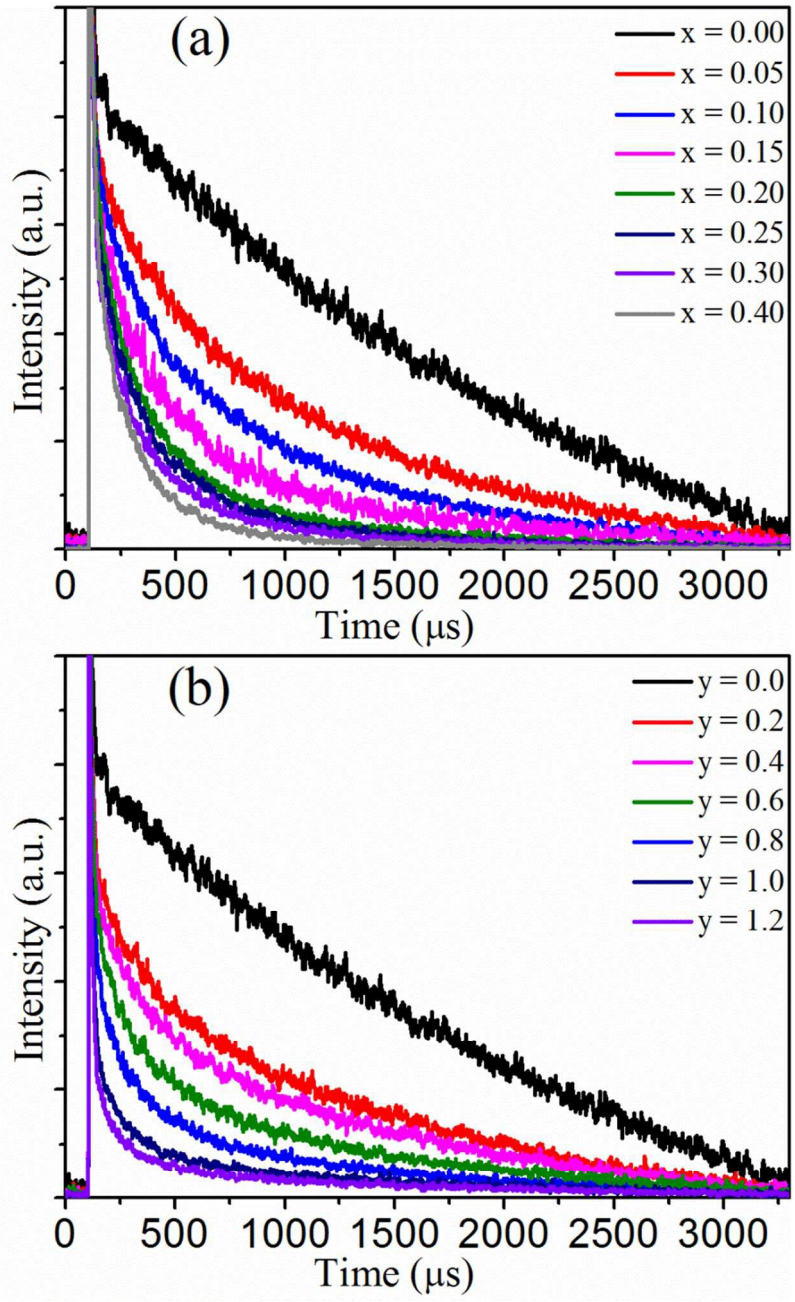

Figure 9. Decay curves of Mn^{4+} luminescence in $Ca_{14-x}Zn_6Al_{9.8}O_{35}$: $Mn_{0.2}$, Nd_x (a)/ $Ca_{14-y}Zn_6Al_{9.8}O_{35}$: $Mn_{0.2}$, Yb_y (b) monitoring at 710 nm excited at 460 nm light.

In order to further understand the energy transfer process and estimate the energy transfer sensitization efficiency, the luminescence decay curves of the Mn^{4+}: $^2E \rightarrow {}^4A_2$ emission were measured in the $Ca_{14-x/y}Zn_6Al_{9.8}O_{35}$: $Mn_{0.2}$, Nd_x/Yb_y (from x = 0.00 to 0.40; from y = 0.0 to 1.2)

samples under excitation at 460 nm, as shown in Figure 9. It can be seen that the decay rate increases with the increase of Nd^{3+}/Yb^{3+} contents. The effective lifetime of the Mn^{4+} luminescence is expressed as

$$\tau = \frac{\int_0^\infty tI(t)dt}{\int_0^\infty I(t)dt}, \quad (1)$$

where $I(t)$ is the time dependent luminescence intensity of Mn^{4+} and τ is the decay lifetime of Mn^{4+} luminescence. The calculated decay lifetimes are all listed in Table 1. It can be seen that the lifetime of Mn^{4+} luminescence decreases monotonously from 1.123 to 0.413 ms with the Nd^{3+} content increasing from 0.00 to 0.40 and from 1.123 to 0.652 ms with the Yb^{3+} content increasing from 0.0 to 1.2. The Nd^{3+}/Yb^{3+} concentration dependence of the decay lifetime proves the nonradiative energy transfer process from Mn^{4+} to Nd^{3+}/Yb^{3+}. The energy transfer efficiency (η_{ET}) can be calculated by[31]

$$\eta_{ET} = 1 - \frac{\tau}{\tau_0}. \quad (2)$$

Where τ and τ_0 are the lifetimes of the Mn^{4+} luminescence in the Mn^{4+}, Nd^{3+}/Yb^{3+} co-doped and Mn^{4+} single-doped cases, respectively. The estimated energy transfer efficiencies are listed in Table 1. As expected, with the increase of Nd^{3+}/Yb^{3+} content, the energy transfer efficiency gradually increases due to the decrease of distance between donor (Mn^{4+}) and acceptor (Nd^{3+}/Yb^{3+}). It should be pointed out that the near infrared emission intensity will decrease when the Nd^{3+}/Yb^{3+} doping concentration exceeds a certain value, although the $Mn^{4+} \rightarrow Nd^{3+}/Yb^{3+}$ energy transfer probability always increases with the enhancement of Nd^{3+}/Yb^{3+} doping

concentration in our experiment. This means that fluorescence quenching is inevitable because of the intensified Nd^{3+}-Nd^{3+} or Yb^{3+}-Yb^{3+} interaction at high Nd^{3+}/Yb^{3+} concentration.

Table 1. The effective decay lifetime (τ) of Mn^{4+} luminescence and the energy transfer efficiency (η_{ET}) of Mn^{4+}→Nd^{3+}/Yb^{3+}.

$Ca_{14-x}Zn_6Al_{9.8}O_{35}$: $Mn_{0.2}$, Nd_x			$Ca_{14-y}Zn_6Al_{9.8}O_{35}$: $Mn_{0.2}$, Yb_y		
Content(x)	τ (ms)	$\eta_{ET(Mn^{4+}\rightarrow Nd^{3+})}$	Content(y)	τ (ms)	$\eta_{ET(Mn^{4+}\rightarrow Yb^{3+})}$
0.00	1.123	0.000	**0.0**	1.123	0.000
0.05	0.901	0.198	**0.2**	0.924	0.177
0.10	0.783	0.303	**0.4**	0.899	0.199
0.15	0.666	0.407	**0.6**	0.806	0.282
0.20	0.575	0.488	**0.8**	0.749	0.333
0.25	0.525	0.533	**1.0**	0.716	0.363
0.30	0.486	0.567	**1.2**	0.652	0.419
0.40	0.413	0.632			

It is known that the energy transfer types include radiation reabsorption, exchange interaction, and multipolar interaction. For the $Ca_{14}Zn_6Al_{10}O_{35}$: Mn^{4+}, Nd^{3+}/Yb^{3+}, the energy transfer based on radiation reabsorption can be neglected because the structure of the emission spectra of Mn^{4+} is hardly changed in $Ca_{14}Zn_6Al_{10}O_{35}$: Mn^{4+}, Nd^{3+}/Yb^{3+} phosphors with Nd^{3+}/Yb^{3+} content increasing (see Figure 10). If the energy transfer takes place by exchange

interaction, the critical distance between the donor and acceptor should be short enough (< 5 Å).[32] The distance (R_C) between the Mn^{4+} and Nd^{3+}/Yb^{3+} ions were estimated with the following equation[33]

$$R_C \approx 2\left[\frac{3V}{4\pi x_C N}\right]^{1/3}. \quad (3)$$

Here x_C is the critical concentration of the doped ions, V is the volume of the unit cell of $Ca_{14}Zn_6Al_{10}O_{35}$ (3286.7 $Å^3$). N is the number of Ca^{2+} ions in the unit cell (N = 86). The critical concentration are estimated to be about 0.032 and 0.107 for the $Ca_{14}Zn_6Al_{10}O_{35}$: Mn^{4+}, Nd^{3+} and $Ca_{14}Zn_6Al_{10}O_{35}$: Mn^{4+}, Yb^{3+} from the total concentration of the Mn^{4+} and Nd^{3+}/Yb^{3+} ions at which the energy transfer efficiency is 50%. Thus by using eq. (3), the critical distances are estimated to be 13.1 Å in $Ca_{14}Zn_6Al_{10}O_{35}$: Mn^{4+}, Nd^{3+} and 8.8 Å in $Ca_{14}Zn_6Al_{10}O_{35}$: Mn^{4+}, Yb^{3+}. These values are all larger than the typical critical distance for exchange interaction (< 5 Å), indicating that the exchange interaction plays an unimportant role in the $Mn^{4+}\rightarrow Nd^{3+}/Yb^{3+}$ energy transfer process. Thus the energy transfer should be performed via electric multipolar interaction.

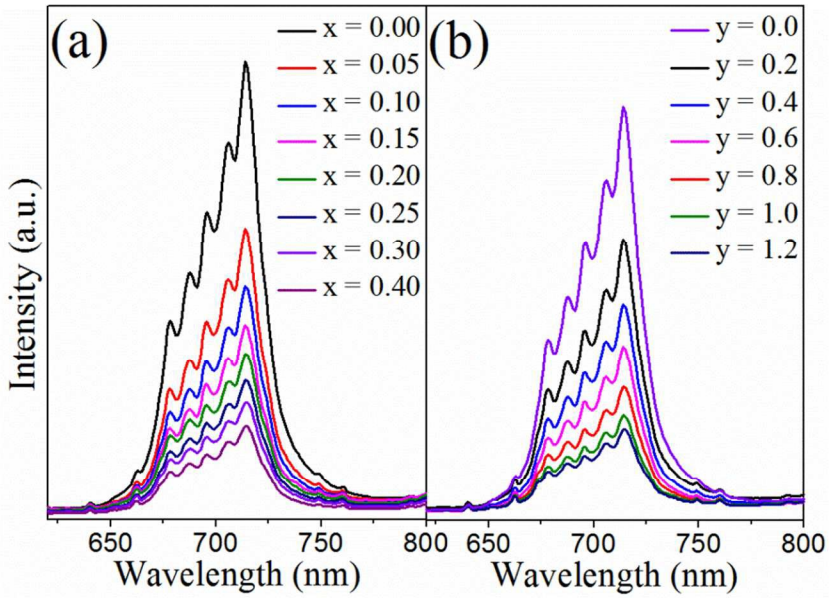

Figure 10. Emission spectra of Mn^{4+} in $Ca_{14-x}Zn_6Al_{9.8}O_{35}$: $Mn_{0.2}$, Nd_x (a)/$Ca_{14-y}Zn_6Al_{9.8}O_{35}$: $Mn_{0.2}$, Yb_y (b) excited at 460 nm light.

Base on Dexter's theory of multipolar interaction and Reisfeld's approximation, the type of multipolar interaction between donor and acceptor ions can be expressed in the following equation:[34-36]

$$\frac{\tau_0}{\tau} \propto C^{n/3} \quad (4)$$

τ_0 and τ are the luminescence decay lifetimes of the donor (Mn^{4+}) in the absence and presence of the acceptor (Nd^{3+}/Yb^{3+}), respectively. C is the acceptor (Nd^{3+}/Yb^{3+}) concentration, and $n = 6$, 8 and 10 represent the dipole-dipole, dipole-quadrupole, and quadrupole-quadrupole interactions, respectively. With the experimental data, the $\tau_0 / \tau - C^{n/3}$ plots are illustrated in Figure 11. The best linear relationship is obtained when $n = 6$ for both Mn^{4+}, Nd^{3+} co-doped and Mn^{4+}, Yb^{3+} co-doped samples, indicating that a dipole-dipole

interaction is predominantly responsible for the energy transfer of Mn^{4+}→Nd^{3+}/Yb^{3+}.

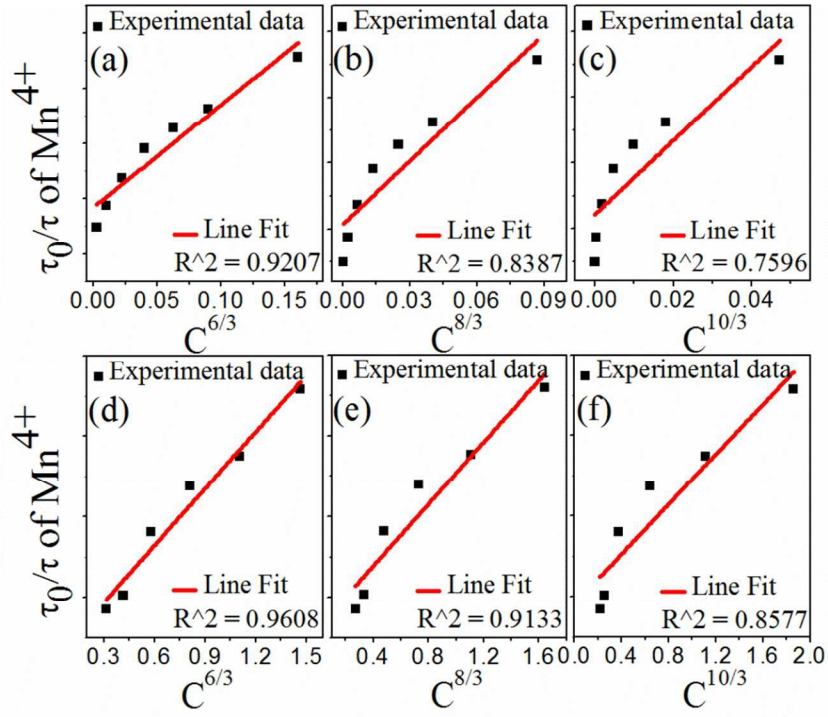

Figure 11. Dependence of τ_0/τ of Mn^{4+} on $Ca_{14}Zn_6Al_{10}O_{35}$: Mn^{4+}, Nd^{3+} (a, b, c)/$Ca_{14}Zn_6Al_{10}O_{35}$: Mn^{4+}, Yb^{3+} (d, e, f) at $C^{6/3}$, $C^{8/3}$, and $C^{10/3}$, respectively.

The luminescence decay curves of Mn^{4+} can also be further analyzed by the generalized Yokota-Tanimoto (Y-T) model:[37, 38]

$$I(t) = I(0)\exp\left(-\frac{t}{\tau_0} - \frac{4\pi}{3}C\Gamma\left(1-\frac{3}{S}\right)\left(C_{DA}^{(S)}t\right)^{3/S} \times\left(\frac{1+a_1X+a_2X^2}{1+b_1X}\right)^{S-3/S-2}\right), \quad (5)$$

with $X = D\left(C_{DA}^{(S)}\right)^{-2/S} t^{1-2/S}$, where τ_0 is the decay constant of the donor (Mn^{4+}) luminescence in the single-doped sample, S is the parameter of multipolar interaction that represents the dipole-dipole ($S=6$), dipole-quadrupole ($S=8$), and quadrupole-quadrupole ($S=10$)

interactions, respectively. C is the acceptor (Nd^{3+}/Yb^{3+}) concentration. $\Gamma(x)$ is the gamma function, and $C_{DA}^{(S)}$ is the donor-acceptor energy transfer parameter. a_i and b_i are the approximant coefficients involved in the electric multipolar interaction. D is the diffusion parameter that characterizes the excitation diffusion among donor ions. In principle, the excited donor ions can transfer their energy to the acceptor ions directly, or after the energy transfer between the nearest donor ions via excitation diffusion until an acceptor ion is reached. It is found in our experiment that the luminescence decay curves of Mn^{4+} in Mn^{4+} single-doped samples almost have no change as Mn^{4+} doping content increases from z = 0.2 to 0.6, as shown in Figure 12(a). The result indicates that the Mn^{4+} radiation decay curve is mainly determined by its spontaneous emission of the isolated Mn^{4+} ions and the diffusion among the Mn^{4+} ions is of no importance. Thus the diffusion parameter of D can be set to 0. In this generalized Y-T model, the obtained best fitting is at $S = 6$ for Mn^{4+}, Nd^{3+} co-doped and Mn^{4+}, Yb^{3+} co-doped samples, as shown in Figure 12(b) and 12(c). This further indicates the energy transfer between the Mn^{4+} and Nd^{3+}/Yb^{3+} ions is performed via dipole-dipole interaction.

The SEM images of the $Ca_{13.75}Zn_6Al_{9.4}O_{35}$: $Mn_{0.6}$, $Nd_{0.25}$ and $Ca_{13.2}Zn_6Al_{9.4}O_{35}$: $Mn_{0.6}$, $Yb_{0.8}$ phosphors are shown in Figure 13(a) and 13(b). The phosphors present coherent flake structure. Thus they are likely to be fabricated onto the front surface of solar cells as planar down-shifting layer (shown in Figure 13(c)). Based on eq. (1) and (2), it is found that the calculated energy transfer efficiency for the $Ca_{13.75}Zn_6Al_{9.4}O_{35}$: $Mn_{0.6}$, $Nd_{0.25}$ and $Ca_{13.2}Zn_6Al_{9.4}O_{35}$: $Mn_{0.6}$, $Yb_{0.8}$ samples are as high as 76.0% and 80.4%, respectively. Moreover, the integrated NIR

luminescent intensity of Yb^{3+} is 1.12 orders higher than that of Nd^{3+} in $Ca_{13.75}Zn_6Al_{9.4}O_{35}$: $Mn_{0.6}$, $Nd_{0.25}$ and $Ca_{13.2}Zn_6Al_{9.4}O_{35}$: $Mn_{0.6}$, $Yb_{0.8}$ under same excitation conditions (excited by 460 nm light) and the Si-based solar cell is more sensitive to the 980 nm light emitted by Yb^{3+} than the 900, 1060 nm light emitted by Nd^{3+}. Thus the $Ca_{13.2}Zn_6Al_{9.4}O_{35}$: $Mn_{0.6}$, $Yb_{0.8}$ phosphor might be more suitable for spectral down-shifting application.

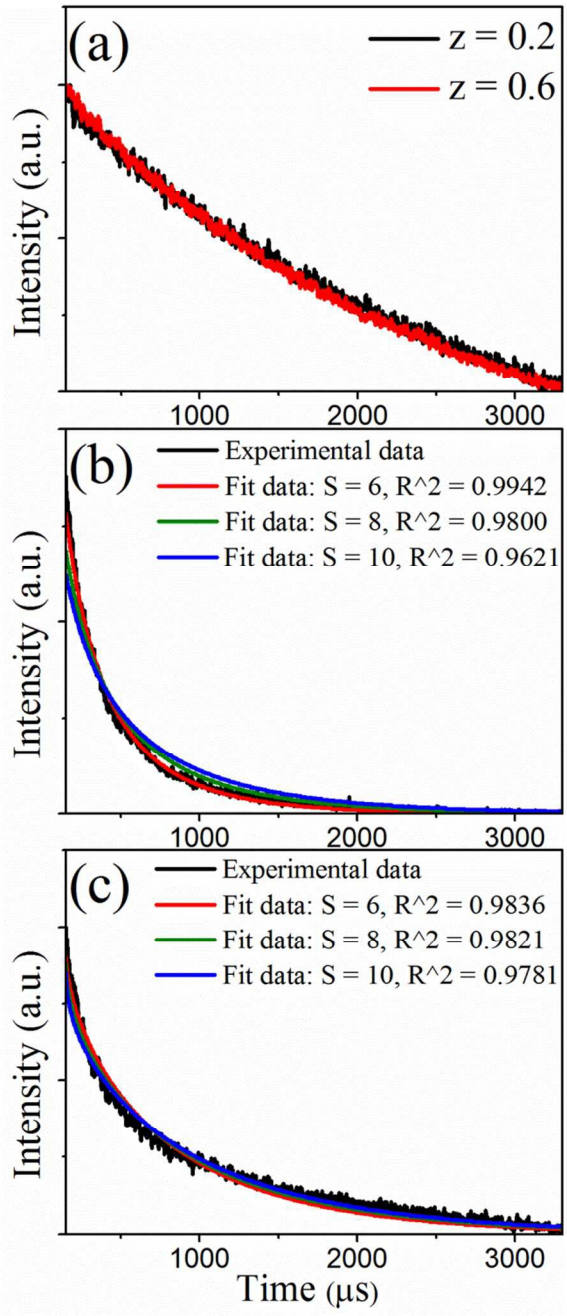

Figure 12. Decay curves of Mn^{4+} luminescence for $Ca_{14}Zn_6Al_{10-z}O_{35}$: Mn_z (z = 0.2, 0.6) (a), decay curves of Mn^{4+} luminescence and its fitted curves based on Y-T model for $Ca_{13.75}Zn_6Al_{9.8}O_{35}$: $Mn_{0.2}$, $Nd_{0.25}$ (b) and for $Ca_{13.2}Zn_6Al_{9.8}O_{35}$: $Mn_{0.2}$, $Nd_{0.8}$ (c). The decay curves are recorded at 710 nm emission under excitation at 460 nm.

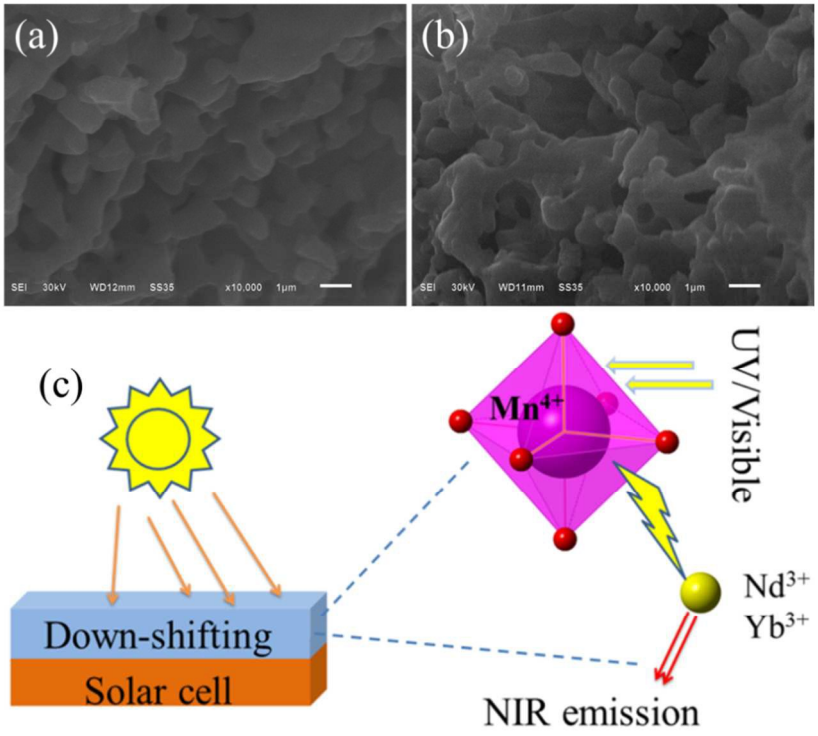

Figure 13. SEM images of $Ca_{13.75}Zn_6Al_{9.4}O_{35}$: $Mn_{0.6}$, $Nd_{0.25}$ (a) and $Ca_{13.2}Zn_6Al_{9.4}O_{35}$: $Mn_{0.6}$, $Yb_{0.8}$ (b) and schematic diagram of down-shifting layer (c).

4. CONCLUSIONS

In summary, novel NIR phosphors of $Ca_{14}Zn_6Al_{10}O_{35}$: Mn^{4+}, Nd^{3+}/Yb^{3+} with high-efficiency are prepared. The $Ca_{14}Zn_6Al_{10}O_{35}$: Mn^{4+}, Nd^{3+}/Yb^{3+} phosphors exhibit strong absorption due to the Mn^{4+}-O^{2-} charge transfer transition and Mn^{4+} (3d)-electronic spin-allowed transitions and give intense near infrared emission caused by the energy transfer from Mn^{4+} to Nd^{3+}/Yb^{3+}. It means that the phosphors can possibly be used as spectral conversion materials to enhance the efficiency of Si-based solar cells. The spectral conversion mechanism is investigated in detail according to their excitation-emission spectra and luminescence decay performance.

The dipole-dipole interaction induced energy transfers are responsible for the strong NIR emission of Nd^{3+}/Yb^{3+} under the excitation of the light ranging from 250 to 550 nm.

ACKNOWLEDGMENTS

This work was supported by the National Science Foundation of China (No. 51372214 & 61233010), Project of Department of Science and Technology of Hunan Province of China (No. 2014FJ3124), and the Open Project of State Key Laboratory of Rare Earth Resources Utilization, Changchun Institute of Applied Chemistry, Chinese Academy of Science (RERU2013017).

Notes and references

Corresponding Author

* Electronic mail: xiaosiguo@xtu.edu.cn

Notes

The authors declare no competing financial interest.

REFERENCES

1 B. M. van der Ende, L. Aarts and A. Meijerink, Lanthanide ions as spectral converters for solar cells, *Phys. Chem. Chem. Phys.,* 2009, ***11***, 11081-11095.

2 B. Fan, C. Chlique, O. Merdrignac-Conanec, X. Zhang and X. Fan, Near-Infrared Quantum Cutting Material Er^{3+}/Yb^{3+} Doped La_2O_2S with an External Quantum Yield Higher than 100%, *J. Phys. Chem. C,* 2012, ***116***, 11652-11657.

3 B. S. Richards, Luminescent layers for enhanced silicon solar cell performance: Down-conversion, *Solar Energy Materials and Solar Cells,* 2006, ***90***, 1189-1207.

4 T. Trupke, M. A. Green and P. Würfel, Improving solar cell efficiencies by down-conversion of high-energy photons, *J. Appl. Phys.,* 2002, ***92***, 1668.

5 T. C. Liu, G. Zhang, X. Qiao, J. Wang, H. J. Seo, D. P. Tsai and R. S. Liu, Near-Infrared Quantum Cutting Platform in Thermally Stable Phosphate Phosphors for Solar Cells, *Inorg. Chem.,* 2013, ***52***, 7352-7357.

6 Y. Teng, J. Zhou, X. Liu, S. Ye and J. Qiu, J. Efficient broadband near-infrared quantum cutting for solar cells, *Opt. Express,* 2010, ***18***, 9671-9676.

7 S. Ye, J. Zhou, S. Wang, R. Hu, D. Wang and J. Qiu, Broadband downshifting luminescence in Cr^{3+}-Yb^{3+} codoped garnet for efficient photovoltaic generation, *Opt. Express,* 2013, ***21***, 4167-4173.

8 G. Gao and L. Wondraczek, Near-infrared down-conversion in Mn^{2+}-Yb^{3+} co-doped Zn_2GeO_4, *J. Mater. Chem. C,* 2013, ***1***, 1952-1958.

9 P. Liu, J. Liu, X. Zheng, H. Luo, X. Li, Z. Yao, X. Yu, X. Shi, B. Hou and Y. Xia, An efficient light converter YAB: Cr^{3+}, Yb^{3+}/Nd^{3+} with broadband excitation and strong NIR emission for harvesting c-Si-based solar cells, *J. Mater. Chem. C,* 2014, ***2***, 5769-5777.

10 G. V. Shcherbatyuk, R. H. Inman, C. Wang, R. Winston and S. Ghosh, Control of growth and the processes of energy transfer from CdSe quantum dots for Nd^{3+} ions in a vitreous system: Thermal annealing time, *Appl. Phys. Lett.,* 2012, ***101***, 121903.

11 C.-C. Lin, H.-C. Chen, Y. L. Tsai, H.-V. Han, H.-S. Shih, Y.-A. Chang, H.-C. Kuo and P. Yu, Incorporation and Luminescence of Yb^{3+} in CdSe Nanocrystals, *J. Am. Chem. Soc.,* 2013, ***135***, 13668-13671.

12 X. Pi, Q. Li, D. Li and D. Yang, Luminescence of Nd^{3+} ions under excitation of CdSe quantum dots in a glass system: energy transfer, *Opt. Lett.,* 2014, **39**, 131-134.

13 K. Seki, K. Uematsu, K. Toda and M. Sato, Novel Deep Red Emitting Phosphors $Ca_{14}Zn_6M_{10}O_{35}$: Mn^{4+} (M = Al^{3+} and Ga^{3+}), *Chem. Lett.,* 2014, ***43***, 1213-1215.

14 M. Peng, X. Yin, P. A. Tanner, M. G. Brik and P. Li, Site Occupancy Preference, Enhancement Mechanism, and Thermal Resistance of Mn^{4+} Red Luminescence in $Sr_4Al_{14}O_{25}$: Mn^{4+} for Warm WLEDs, *Chem. Mater.,* 2015, ***27***, 2938-2945.

15 M. G. Brik and A. M. Srivastava, On the optical properties of the Mn^{4+} ion in solids, *J. Lumin.,* 2013, ***133***, 69-72.

16 B. Wang, H. Lin, J. Xu, H. Chen and Y. Wang, $CaMg_2Al_{16}O_{27}$: Mn^{4+}-based Red Phosphor: A Potential Color Converter for High-Powered Warm W-LED, *ACS Appl. Mater. Interfaces,* 2014, ***6***, 22905-22913.

17 L. Meng, L. Liang and Y. Wen, Deep red phosphors $SrMgAl_{10}O_{17}$: Mn^{4+}, M (M = Li^+, Na^+, K^+, Cl^-) for warm white light emitting diodes, *J. Mater. Sci.: Mater. Electron.,* 2014, ***25***,

2676-2681.

18 S. Okamoto and H. Yamamoto, Luminescent-Efficiency Improvement by Alkaline-Earth Fluorides Partially Replacing MgO in $3.5MgO{\cdot}0.5MgF_2{\cdot}GeO_2$: Mn^{4+} Deep-Red Phosphors for Light Emitting Diodes, *J. Electrochem. Soc.,* 2010, ***157***, J59-J63.

19 M. Peng, X. Yin, P. A. Tanner, C. Liang, P. Li, Q. Zhang, J. Qiu and A. Srivastava, Orderly-Layered Tetravalent Manganese-Doped Strontium Aluminate $Sr_4Al_{14}O_{25}$: Mn^{4+}: An Efficient Red Phosphor for Warm White Light Emitting Diodes, *J. Am. Ceram. Soc.,* 2013, ***96***, 2870-2876.

20 C. Liao, R. Cao, Z. Ma, Y. Li, G. Dong, K. N. Sharafudeen, J. Qiu and J. Heo, Synthesis of K_2SiF_6: Mn^{4+} Phosphor from SiO_2 Powders via Redox Reaction in $HF/KMnO_4$ Solution and Their Application in Warm-White LED, *J. Am. Ceram. Soc.,* 2013, ***96***, 3552-3556.

21 M. M. Medić, M. G. Brik, G. Dražić, Ž. M. Antić, V. M. Lojpur and M. D. Dramićanin, Deep-Red Emitting Mn^{4+} Doped Mg_2TiO_4 Nanoparticles, *J. Phys. Chem. C,* 2015, ***119***, 724-730.

22 W. Lu, W. Lv, Q. Zhao, M. Jiao, B. Shao and H. You, A Novel Efficient Mn^{4+} Activated $Ca_{14}Al_{10}Zn_6O_{35}$ Phosphor: Application in Red-Emitting and White LEDs, *Inorg. Chem.,* 2014, ***53***, 11985-11990.

23 M. H. Du, Chemical trends of Mn^{4+} emission in solids, *J. Mater. Chem. C,* 2014, ***2***, 2475-2481.

24 V. Barbanyagre, T. Timoshenko, A. Ilyinets and V. Shamshurov, Calcium aluminozincates of $Ca_xAl_yZn_kO_n$ composition, *Powder Diffr.,* 1997, ***12***, 22-26.

25 J. Carver, G. Schweitzer and T. A. Carlson, Use of X-Ray photoelectron spectroscopy to study bonding in Cr, Mn, Fe, and Co compounds, *J. Chem. Phys.*, 1972, ***57***, 973-982.

26 J. Zhou, Y. Teng, X. Liu, S. Ye, X. Xu, Z. Ma and J. Qiu, Intense infrared emission of Er^{3+} in $Ca_8Mg(SiO_4)_4Cl_2$ phosphor from energy transfer of Eu^{2+} by broadband down-conversion, *Opt. Express*, 2010, ***18***, 21663-21668.

27 V. Singh, R. P. S. Chakradhar, I. Ledoux-Rak, L. Badie, F. Pelle and S. Ivanova, Infrared and visible emission of Er^{3+} in combustion-synthesized $CaAl_2O_4$ phosphors, *J. Lumin.*, 2009, ***129***, 1375-1380.

28 J. Lü, Y. Huang, Y. Tao and H. J. Seo, Spectroscopic parameters of Ce^{3+} ion doped $Na_2CaMg(PO_4)_2$ phosphor, *J. Alloys Compd.*, 2010, ***500***, 134-137.

29 L. Lv, X. Jiang, S. Huang, X. a. Chen and Y. Pan, The formation mechanism, improved photoluminescence and LED applications of red phosphor K_2SiF_6: Mn^{4+}, *J. Mater. Chem. C,* 2014, ***2***, 3879-3884.

30 T. Miyakawa and D. L. Dexter, Multiphonon Relaxation of Excited States, and Phonon-Assisted Energy Transfer between Ions in Solids, *Phys. Rev. B,* **1970**, *1*, 2961-2969.

31 P. Paulose, G. Jose, V. Thomas, N. Unnikrishnan and M. Warrier, Sensitized fluorescence of Ce^{3+}/Mn^{2+} system in phosphate glass, *J. Phys. Chem. Solids,* 2003, ***64***, 841-846.

32 D. L. Dexter, A Theory of Sensitized Luminescence in Solids, *J. Chem. Phys.,* 1953, ***21***, 836.

33 G. Blasse, Energy transfer in oxidic phosphors, *Phys. Lett. A,* 1968, ***28***, 444-445.

34 D. Dexter and J. H. Schulman, Theory of Concentration Quenching in Inorganic Phosphors,

J. Chem. Phys., 1954, ***22***, 1063.

35 R. Reisfeld, Luminescence Quantum Efficiency of Gd and Tb in Borate Glasses and the Mechanism of Energy Transfer between Them, *J. Chem. Phys.,* 1972, ***56***, 1698.

36 Z. G. Nie, J. H. Zhang, X. Zhang, S. Z. Lü, X. G. Ren, G. B. Zhang and X. J. Wang, Photon cascade luminescence in $CaAl_{12}O_{19}$: Pr, Cr, *J. Phys. Chem. Solids,* 2007, ***180***, 2933-2941.

37 K. Allinger and A. Blumen, On the direct energy transfer to moving acceptors, *J. Chem. Phys.,* 1980, ***72***, 4608.

38 I. R. Martín, V. D. Rodríguez, U. R. Rodríguez-Mendoza, V. Lavín, E. Montoya and D. Jaque, Energy transfer with migration. Generalization of the Yokota-Tanimoto model for any kind of multipole interaction, *J. Chem. Phys.,* 1999, ***111***, 1191.